

Development of a low-cost plasma source using fly-back transformer for atmospheric pressure gliding arc discharge

Cite as: Phys. Plasmas 31, 043509 (2024); doi: 10.1063/5.0187159

Submitted: 11 November 2023 · Accepted: 2 April 2024 ·

Published Online: 18 April 2024



View Online



Export Citation



CrossMark

Sangat Sharma,¹ Roshan Chalise,^{1,2} Suresh Basnet,^{1,a)} Hari Prasad Lamichhane,¹ and Raju Khanal^{1,b)}

AFFILIATIONS

¹Central Department of Physics, Tribhuvan University, Kirtipur, Kathmandu 44613, Nepal

²Department of Physics, Amrit Campus, Tribhuvan University, Kathmandu 44600, Nepal

^{a)}Author to whom correspondence should be addressed: sbplasma1986@gmail.com

^{b)}Electronic mail: raju.khanal@cdp.tu.edu.np

ABSTRACT

This study outlines the development of a cost-effective power supply tailored for generating atmospheric pressure gliding arc discharge, primarily for non-thermal plasma processes. We conduct a comprehensive analysis of discharge characteristics using optical and electrical methods, focusing on parameters such as discharge temperature, plasma density, and current-voltage characteristics. The output voltage (V_{RMS}) of the power supply increases within the range of (7.67 ± 0.41) to (26.71 ± 0.88) kV. Our findings indicate that arc velocity increases with the increase in airflow rate, whereas it is reduced with the increase in applied voltage. The power consumption of the discharge falls within 8.55–18.34 W for applied voltages ranging from 12.00 to 20.00 V. The electron temperature and density decrease toward the electrode outlet, with values of 1.194 ± 0.024 eV and $(0.66 \pm 0.17) \times 10^{17} \text{ cm}^{-3}$, respectively, at the outermost region. Variations in applied voltage affect both electron temperature and density. Additionally, airflow and applied voltage influence rotational and vibrational temperatures, with maximum values observed at the lowermost equilibrium position for increased airflow. Our findings demonstrate a non-thermodynamic equilibrium discharge, as evidenced by the fact that the electron temperature exceeds vibrational temperature and vibrational temperature exceeds rotational temperature. The suggested techniques are both practical and efficient, with a straightforward construction process, and have been demonstrated to be applicable in the agricultural field.

© 2024 Author(s). All article content, except where otherwise noted, is licensed under a Creative Commons Attribution (CC BY) license (<https://creativecommons.org/licenses/by/4.0/>). <https://doi.org/10.1063/5.0187159>

I. INTRODUCTION

Plasma, a highly ionized state of matter consisting of electrons, ions, and neutral species in local electric neutrality, distinguishes itself from ordinary gas. While naturally occurring in phenomena such as Aurora, lightning bolts, stars, and interplanetary media, plasma is also artificially produced by ionizing neutral gases at low pressure and high temperature.¹ Plasma is categorized into thermal and non-thermal plasma, with various subcategories based on electron and ion densities and temperatures, plasma holds significant importance across multiple domains. Thermal plasma, characterized by high energy density and near-equilibrium electron and ion temperatures ($T_e \approx T_i \approx T_g$), finds extensive use in waste material treatment, chemical vapor deposition, metallurgy, aerospace, and microelectronics.²

On the other hand, non-thermal plasma (NTP), commonly referred to as “cold plasma,” exhibits lower energy density compared

to thermal plasma. With electron temperatures typically up to 10 eV, NTP sustains high electron temperature while keeping overall gas temperature near room temperature, owing to its low electron density.³ Non-thermal atmospheric pressure plasma (NTAPP), generated at atmospheric pressure, has garnered considerable attention for its diverse applications in agriculture,⁴ bio-medicine,⁵ and material processing.⁶ Its generation involves supplying energy to a neutral gas to induce the formation of charge carriers, typically achieved through the application of an electric field, which accelerates charge carriers within the plasma.⁷ Various non-thermal electrical discharges, such as arc discharge, glow discharge, and dielectric barrier discharge, contribute to plasma generation across specific applications. These discharges facilitate the ionization of molecules and atomic gases, leading to the formation of free radicals and excited atoms.⁸ Subsequently, reactive oxygen and nitrogen species produced in this process hold significant promise

in food processing,⁹ microbial deactivation,¹⁰ seed germination enhancement,¹¹ and material surface modification.^{12,13}

Among these methods, gliding arc discharge (GAD) emerges as an environmentally friendly approach for generating non-thermal, non-equilibrium atmospheric pressure plasma, showcasing efficiency in chemical reactions and material surface treatment.^{14,15} Originally developed to enhance chemical reactions and gas treatment processes, GAD has emerged as a versatile tool with applications in various fields.¹⁵ The clean energy generation potential of GAD surpasses the conventionally used bio-fuel and chemical-based methods. Additionally, GAD is found to be orders of magnitude more efficient than dielectric barrier discharges and other thermal plasma sources due to its unique characteristics: higher efficiency, larger volume, and operation under highly non-equilibrium conditions characterized by high electron temperature and low ion temperature.^{15–17} It can achieve electron temperatures as high as 10 eV while maintaining the average gas kinetic temperature as low as 0.04 eV.¹⁸ The high-temperature electron can easily disassociate the chemical bonds of stable atoms and molecules to initiate the reaction while mitigating the negative effects of high gas temperature, thus expanding the utilization of plasma in chemical industries.^{1,19}

A GAD setup typically consists of two or more diverging electrodes arranged vertically. Fast-moving gas is injected at one end, initiating an arc at the shortest distance between the electrodes. This arc then glides along the elongated gap, propelled by the gas flow. The arc length depends on factors like applied power, gas flow rate, and electrode configuration. As the arc reaches the wider end the current path increases, triggering its replacement by a shorter arc at the narrower end again.^{16,20} The electrical energy is transferred to the gas, creating electrons, ions, and other reactive species.²¹ In recent years, gliding arc discharge has gained significant attention for its varied applications, including disinfecting bacteria, treating wastewater, promoting seed growth and enhancing productivity, overheating steam and other gases/flames, and modifying material surfaces.^{22–25} GAD's extensive use is attributed to its versatility in root mean square voltage (V_{RMS}) configuration, its openness, and the ability to manipulate the working gas. GAD can provide the required selective non-equilibrium plasma for various chemical processes at lower temperatures. By using reactive gases, GAD creates a non-equilibrium and dynamic environment that promotes specific chemical reactions. Approximately 80% of the applied power directly contributes to the reaction, and the average residency time of reactive species in the plasma region can be adjusted by regulating the airflow. These unique characteristics enable GAD to typically outperform chemical and thermal techniques by a factor of four orders of magnitude.²⁶

Despite significant advancements, there remains ample room for further research and development in plasma sources to meet the demands of evolving technological applications.⁷ Several studies have been conducted on gliding arc discharge production^{26–28} and characterization,^{28,29} with a primary focus either on generation or on characterization. The pursuit of low-cost, sustainable plasma power sources continues to intrigue the scientific community, with a focus on enhancing accessibility and expanding plasma applications.^{11,29} This paper presents a comprehensive study on designing, constructing, and characterizing gliding arc discharge, focusing on its electrical, optical, and physical characteristics. We provide a comprehensive guide for constructing the reactor using readily available materials found locally,

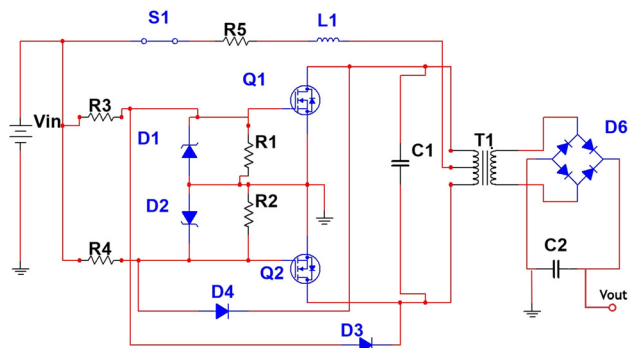


FIG. 1. Electrical circuit (oscillator and voltage step-up section) block diagram of assembled power supply.

resulting in costs of approximately one-tenth of those associated with commercial alternatives. Our methods, proven applicable in agricultural applications,^{11,30} offer practical, efficient, and accessible solutions for harnessing plasma technology.

II. MATERIAL AND METHODS

A. Power supply construction

In this work, we have assembled a pulsed DC power supply using locally available materials with power up to 1 kW (with enough input power) having soft start functionality. This power supply has three sections: power supply section, oscillator section, and voltage step-up section. The power supply section usually has a DC power supply of about 12–50 V, which can supply current up to 25 A. The electrical circuit diagram of the oscillator section and voltage step-up section is shown in Fig. 1 and the used electronic components are listed in Table I. The power supply is based on the Royer oscillator circuit.³¹ This circuit has the advantage of automatically adjusting its oscillation frequency to the resonant frequency, based on the oscillator configuration. Otherwise, a complex mechanism would be required to do this job.³² In addition to the aforementioned advantages, this driver also steps down the reflected voltage and protects the driver circuit. Moreover, the switch remains in an “OFF” state during output and it is easy to control the output voltage and current as well.^{33,34} The circuit (oscillator section, and voltage step-up) was initially designed by Vladimiro Mazzilli. The Mazzilli driver is modified to make it capable of variable frequency, variable voltage, soft-start, and current limiting output. The circuit is self-oscillatory and drives the primary

TABLE I. Detail of the electronic parts used in the driver circuit.

S. No.	Symbol	Part type	Value	Remarks
1	D1, D2	Zener diode	12 V, 1 A	1N4742A
2	D3, D4	Fast diode	1000 V, 3 A	FR307
3	Q1, Q2	Power MOSFET	600 V Vds	IRFP260N
4	R1, R2	Resistors	10 kΩ	0.25 W
5	R3, R4	Resistors	470 Ω	2 W
6	C1	Capacitor	0.68 μF	MKP type
7	L1	Inductor	163 μH	Ferrite core

high-voltage transformer very efficiently. The secondary transformer contains a significantly higher number of turns than the primary.³⁵

Two powerful metal-oxide-semiconductor field-effect transistors (MOSFETs) Q1 and Q2 are the main switching components of this circuit. The gate current of two MOSFETs is controlled by two 2 W resistors R3 and R4 ($470\ \Omega$) with 5% tolerance. The gate voltage on each MOSFET is limited by a 12 V Zener diode for the protection of MOSFETs. The inductor L1 is used to filter out AC components of the oscillator to another part of the circuit and the main power source. The primary winding and capacitor combine to form an inductor-capacitor (LC) tank circuit with a frequency given by

$$f = \frac{1}{2\pi} \sqrt{\frac{1}{LC_1} - \frac{R_L^2}{L^2}}, \quad (1)$$

where L is the inductance of the primary coil and C_1 is the capacitance of the capacitor, and R_L is the resistance of the primary coil. Power is supplied to the circuit by a DC power supply of 24 V and 10 A current. This power is used to switch the MOSFETs and to supply energy to the tank circuit. The tank circuit is composed of a capacitor C1 and the primary coil of the transformer as an inductor. The operational mechanism of the provided circuit is straightforward. Initially, assuming no application is applied to the circuit, both MOSFETs are in the off state, and no energy is being stored or transferred to the secondary winding. When a sufficient voltage is applied to the applied section of the electrical circuit; the gates of both MOSFETs are charged through resistors R3 and R4. As the source of the MOSFET is already grounded, the gate-source junction becomes forward-biased, causing one of the MOSFETs (Q1) to saturate faster than the other (Q2). Once Q1 is saturated, the diode D4 is forward biased, and the gate of the other MOSFET (Q2) is reverse biased keeping the MOSFET Q2 in a cutoff state. During this process, energy is stored in the inductor and starts charging the capacitor. When the capacitor is fully charged, it discharges through the inductor, resulting in oscillation. During the oscillation, the drain of the first MOSFET becomes negative and the second MOSFET's drain becomes positive. During the oscillation, diode D3 becomes forward-biased, while D4 becomes reverse-biased. Consequently, the gate-source junction of MOSFET Q1 becomes reverse biased and turns off, while diode D3 becomes forward biased, and the gate-source junction of Q2 becomes forward biased, turning on the MOSFETs. Now, the current flows in the opposite direction to charge capacitor C1. Once again, when the polarity of the discharge reverses, MOSFET Q1 begins conducting. This process repeats at the resonance frequency of the tank circuit. As the current direction through the inductor (primary winding of the high voltage transformer) changes, energy is transformed to the secondary winding, boosting the voltage, and reducing the current.

A high voltage transformer is constructed by two pieces of "U" shaped ferrite core and it is suitable for high-frequency power transformers since power loss in the normal iron core is very high at kHz frequency. We have re-used the secondary coil of the fly-back transformer with 1205 turns of 26 American wire gauge (AWG) enamel-coated copper wire as secondary winding. Several layers of windings are used, each separated by an insulating wall. A bridge rectifier and a capacitor are used to convert the AC voltage from secondary windings to DC. The transformer's primary coil is center-tapped with eight turnings of 18 AWG enamel-coated copper wire in each section.

B. Generation and characterization of atmospheric pressure plasma

The atmospheric pressure gliding arc discharge is generated using this assembled power supply. The experimental arrangement for the generation of GAD and its electrical and optical characterization methods is shown in Fig. 2. Two copper rod electrodes, each of 5.0 mm in diameter, separated by 3.0 mm in inlet position with a 5.0 mm gap at outlet position having a length of 139.0 mm. The voltage across gliding arc discharge is measured using a $1000\times$ voltage probe (PINTEK HVP-40) and an oscilloscope (Tektronix TBS 1052B). A $100\ \Omega$ resistor is connected in series with the ground (Tektronix TPP0051, $10\times$ voltage probe) electrode to measure the discharge current. For optical spectroscopy of discharge is carried out an HR1 spectroscope (ASEQ Instruments Inc., which has a 195–830 nm wavelength range and 0.176 nm spectral resolution) is placed 10.0 mm from the discharge electrode. The spectra are an average of 30 observations with 300 ms of integration time.

The root mean square (RMS) value of the voltage applied across the electrodes (V_{RMS}), current through the plasma (I_{RMS}), and average power drawn by the plasma (P) are calculated as follows:

$$V_{\text{RMS}} = \sqrt{\frac{\int_0^T (V(t))^2 dt}{T}}, \quad (2)$$

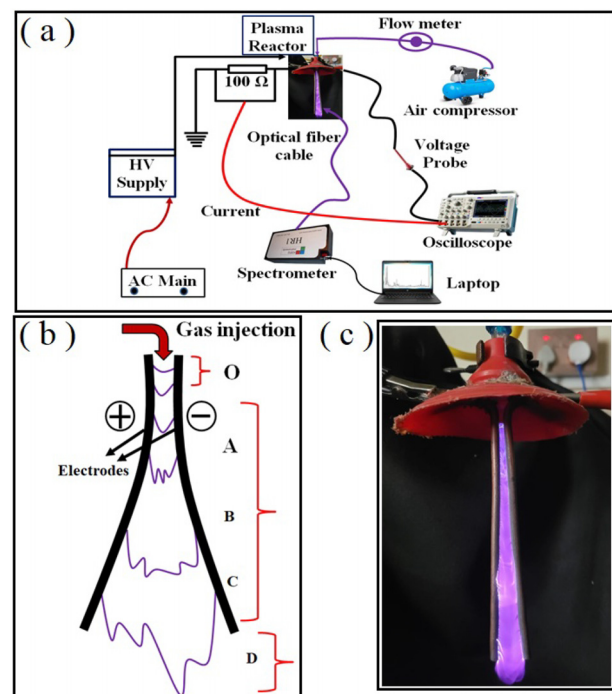


FIG. 2. (a) Schematic diagram for the generation and characterization of the gliding arc discharge, and (b) different regimes of the discharge: "O" is the breakdown region, "A," "B," and "C" represent the equilibrium region, and "D" represents the non-equilibrium region and (c) generation of gliding arc discharge.

$$I_{\text{RMS}} = \sqrt{\frac{\int_0^T (I(t))^2 dt}{T}}, \quad (3)$$

and

$$P = V_{\text{RMS}} \times I_{\text{RMS}}, \quad (4)$$

where t is instantaneous time and T is the time period.

The electron excitation temperature (T_e) is calculated by the Boltzmann plot method of N(III) species, which is taken from the NIST database.³⁶ In this method, the equation for the local thermal equilibrium (LTE) plasma is³⁷

$$\ln \left(\frac{\lambda_{ij} I_{ij}}{A_{ij} g_j} \right) = -\frac{E_j}{k_B T_e} + K, \quad (5)$$

where I_{ij} is the intensity of transition from i to j state, λ_{ij} is the wavelength of transition, A_{ij} is the transition probability, g_j is the statistical weight, E_j is the upper energy level, T_e is the electron excitation temperature, and K is the constant. When we plot the $\ln(\lambda_{ij} I_{ij} / A_{ij} g_j)$ vs E_j , the slope of the obtained graph (Boltzmann plot) gives the electron excitation temperature. The electron density of produced discharge is calculated using the Boltzmann-Saha equation:³⁸

$$n_e = 2 \left(\frac{I_1 \lambda_1 A_2 g_2}{I_2 \lambda_2 A_1 g_1} \right) \left[\frac{2\pi m_e k_B T_e}{h^2} \right]^{\frac{3}{2}} \exp \left[-\frac{E_1 - E_2 + E_i}{k_B T_e} \right]. \quad (6)$$

Here I_1 and I_2 are the intensities of N-III lines, λ_1 and λ_2 are wavelength of neutral and ionized atomic species, A_1 and A_2 are the transition probabilities of neutral and ionized species, g_1 and g_2 are the statistical weight of neutral and ionized species, and E_i is the ionization energy of neutral atom.

The rotational and vibrational temperature of discharge is calculated from the MassiveOES application programming interface (API); open-source, written in the Python language.^{39–41} This code package uses the logarithmic ratio of intensities of different spectral lines to estimate rotational and vibrational temperatures. The experimental emission spectra of N₂ (C-B) molecules are fitted with non-Boltzmann distributions in the spectral wavelength range 306–320 nm. The temperatures are not affected by the spectroscopic distance, or changes in environmental conditions unless there is a variation in the wavelength-specific sensitivity of the spectroscope. The method and the spectral database used to calculate rotational and vibrational temperature are described in previous work.⁴¹

III. RESULTS AND DISCUSSION

A. Power supply characteristics

The temporal evolution of applied and output voltage waveforms across the primary and secondary coils of the transformer is shown in Fig. 3(a). The applied waveform represents the potential difference across the primary winding of the ferrite core transformer, while the output waveform represents the potential difference across the secondary winding of the ferrite core transformer. When the applied DC voltage to the power supply is increased, the primary and secondary voltage of the transformer also linearly increases up to a certain limit. The variation of primary and secondary transformer voltage with the applied DC voltage is shown in Fig. 3(b). There is a strong correlation

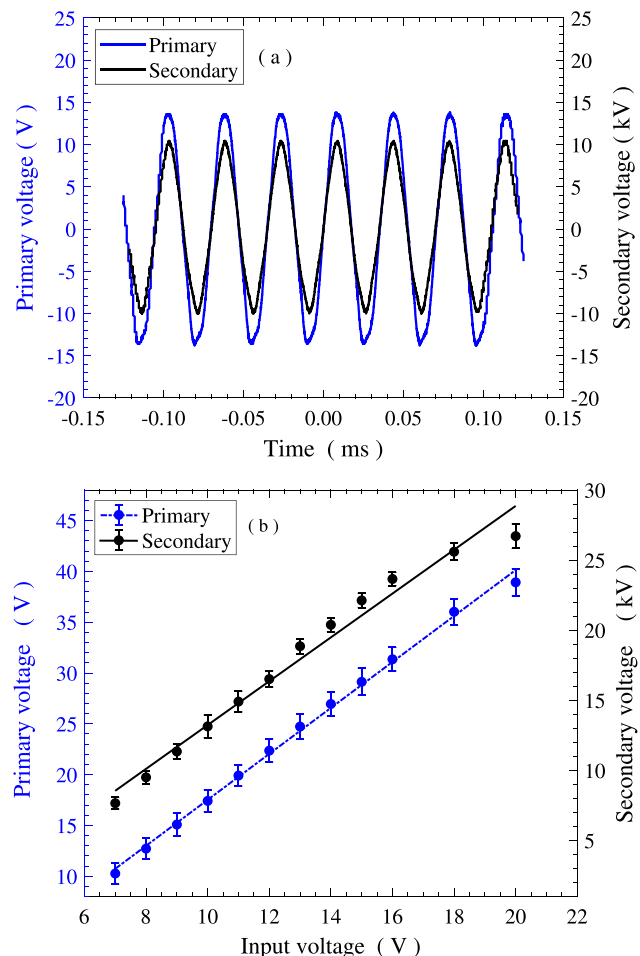


FIG. 3. (a) Primary and secondary voltage waveform and, (b) variation of primary and secondary voltage of transformer as the function of applied voltage.

between applied DC voltage and output AC voltage. The obtained results show that the desired output voltage can be set based on the applied DC voltage. For applied voltage up to 20.00 V, the open-circuit output voltage reaches up to 26.71 ± 0.88 kV (V_{RMS}). This potential is sufficient to generate plasma in different configurations, including dielectric barrier discharge (DBD), gliding arc discharge, plasma jet, and arc discharges.⁴²

When the applied DC voltage increases slowly from 0 to 6.47 V, no oscillation occurs due to the insufficient potential to bias and saturate the working MOSFETs. Beyond 6.47 V applied DC, oscillation occurs with a constant frequency of 32.05 kHz. The primary voltage increases linearly with applied DC voltage and reaches up to 38.92 ± 1.34 V (V_{RMS}) for 20.00 V applied. The secondary voltage of the high-voltage transformer increases linearly from (7.67 ± 0.41) to (26.71 ± 0.88) kV when the input voltage increases from 7.00 to 20.00 V. When the primary input voltage exceeds 16.00 V, the secondary output voltage exceeds 25 kV at which corona discharge can be observed on the pointed parts of the wires and measuring instruments (voltage and current probes). Consequently, the linear increment trend on secondary voltage is disrupted beyond the 16.00 V input.

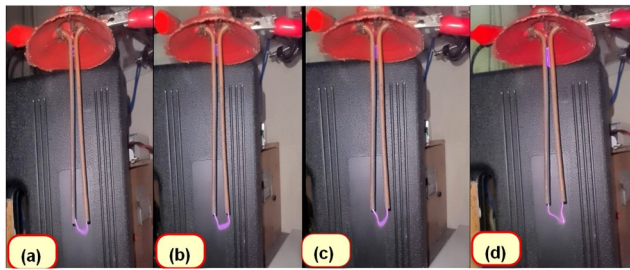


FIG. 4. Picture of single arc at the end point of electrode taken from slow motion camera at constant airflow 15.0 LPM for different values input voltage (a) 12.00 V, (b) 14.00 V, (c) 17.00 V, and (d) 20.00 V.

B. Generation of atmospheric pressure plasma

The assembled power source is used to produce the atmospheric pressure gliding arc discharge. The actual picture of the discharge at the end of the electrodes for different applied voltage values is shown in Fig. 4. As the applied voltage to the reactor increases, the arc length at the end of the electrode also increases. When there is sufficient power, the arc also sustains for a longer time at the end point, decreasing the overall frequency of the arc. The arc is produced at the point with the least distance between electrodes and travels downward due to the downward airflow. During this process, the arc elongates, and the current drawn by the arc increases. The arc eventually dies out, and another arc is initiated. This process repeats with a certain frequency. Airflow rate and speed play an important role in the generation of multiple arcs. Air is blown from the top of the device at a flow rate of 15.0 LPM (liters per minute). Although the gliding arc discharge appears continuous, it is composed of several discrete plasma arcs. The arcs travel downward with a certain velocity at a specific airflow and applied voltage.

The position of the arc at different instances of time is shown in Fig. 5. The pictures are taken by the high-speed camera at 960 frames per second with ISO 3200 and an exposure time of (1/4000)th of a second. The arc glides at high speed as soon as it ignites due to the high velocity of the air at the inlet position (“O” position). As it glides downward, the air expands and the air velocity decreases resulting in lower arc velocity.

C. Arc velocity

Gliding arc velocity is calculated by determining the time taken by the arc to travel from the starting point to the end of the electrodes.

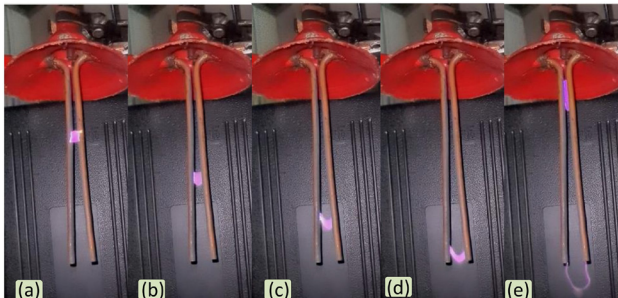


FIG. 5. Position of gliding arc after (a) 8 ms, (b) 16 ms, (c) 24 ms, (d) 32 ms, and (e) 40 ms at 12.00 V input voltage and 15.0 LPM airflow rate.

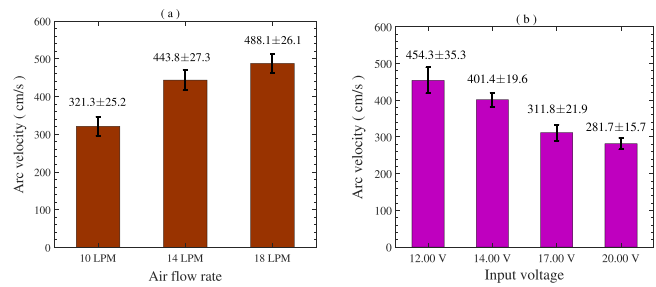


FIG. 6. Arc velocity for different values of (a) air flow rate at constant applied voltage 12.00 V, and (b) applied voltage at constant airflow rate 15.0 LPM.

The gliding velocity of the arc for different air flow rates and applied voltage is shown in Figs. 6(a) and 6(b). The arc velocity gradually increases with the increase in air flow rate, whereas the arc velocity decreases with the increase in applied voltage. As the applied voltage increases, the power drawn by the plasma column also increases; however, the arc velocity decreases. This suggests that both input voltage and power exert a resisting effect on the arc velocity. The measurement of arc velocity during the discharge is crucial to study the effectiveness of gliding arc discharge for various applications.

D. Electrical characterization

The electrical characterization of the plasma gives the information about current and voltage waveform of the produced discharge. The current-voltage characteristics of atmospheric pressure gliding arc discharge for different values of applied DC voltage are shown in Fig. 7. For the generation of gliding arc discharge, the output AC voltage is rectified into pulsating DC voltage, which seems to be more economical and safe because DC voltage can be insulated with dielectrics. Moreover, the corona loss from the sharp points also decreases by using DC voltage. The spikes in the voltage waveform are from the rectified output of the rectifier. As the voltage increases, micro-discharges

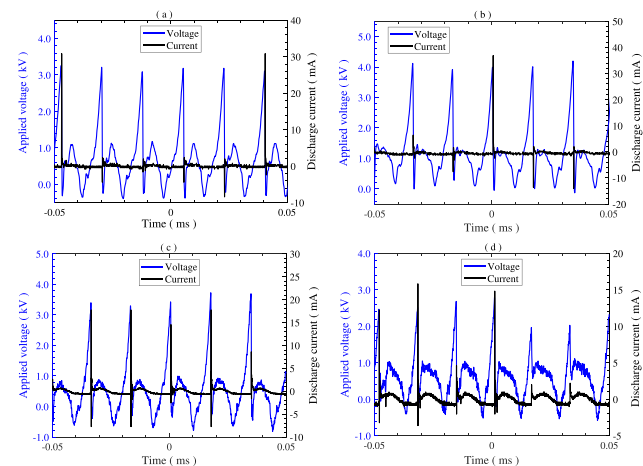


FIG. 7. Current–voltage characteristics of atmospheric air gliding arc discharge at constant airflow rate 15.0 LPM for different values of applied voltage (a) 12.00 V, (b) 14.00 V, (c) 17.00 V, and (d) 20.00 V.

are initiated, causing spikes in the current curve. As the current increases, the voltage decreases sharply, and the cycle repeats. The pulse frequency is twice the AC voltage frequency due to rectification. Increasing the applied DC voltage to the plasma reactor draws more current and, hence, more power.

The first ignition of plasma, i.e., breakdown, occurs at position "O." Immediately after the breakdown, the plasma intensity and current increase, resulting in a sharp decrease in the applied voltage across the two electrodes. As the discharge current increases, a stable plasma channel and the equilibrium regime begin. The gas flow pushes the plasma channel to the other end, elongating the plasma arc. Temperature and arc current do not change drastically in this regime.¹⁶ If the applied current is high enough, this regime becomes longer. In gliding arc discharge, the arcs change position. As a result, the current and voltage values vary markedly and continuously. Therefore, we must consider a complete arc cycle to calculate the power of the discharge.

Figure 8 shows the variation of current and voltage in two complete arc cycles for 12.00 V input. Initially, as the arc ignites, the current rises to the maximum value and the voltage decreases to the lower value. After ignition, as the arc moves downward, the voltage across electrodes increases gradually and the current decreases until the next cycle. The calculated values of RMS current, RMS voltage, and power for different input voltages are tabulated in Table II.

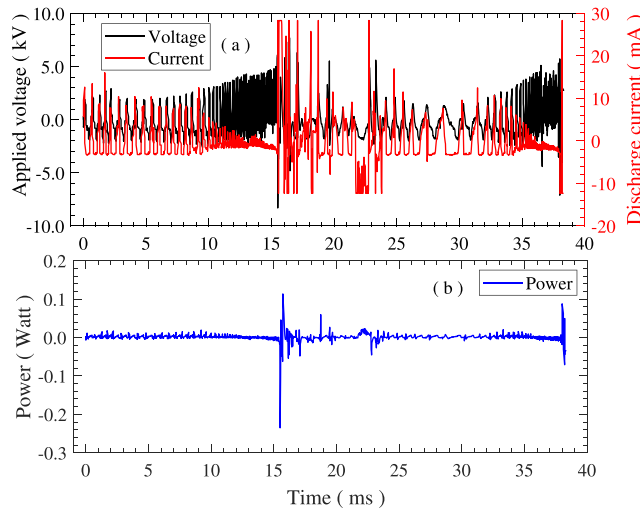


FIG. 8. (a) Current-voltage and (b) power characteristics of the gliding arc discharge of two arc cycles for 12.00 V input voltage and 14.0 LPM airflow.

TABLE II. Calculated values of RMS voltage, RMS current, and power of the plasma reactor for different values of input voltage.

S. No.	Input (V)	V _{RMS} (kV)	I _{RMS} (mA)	P (W)
1	12.00	1.62	5.28	8.55
2	14.00	2.26	5.51	12.45
3	17.00	2.48	5.33	13.22
4	20.00	2.87	6.39	18.34

E. Optical characterization

Optical emission spectroscopy (OES) is a widely used technique to measure the intensity of different wavelengths of light. OES provides valuable information on excited atomic and molecular states to determine the produced discharge's rotational, vibrational, and electron excitation temperature and density. These temperature parameters are important as they directly affect the rate of a chemical reaction during the plasma applications.⁴³ The variation of intensity for increasing the air flow rate and applied voltage are shown in Figs. 9 and 10 respectively. The major observed spectra are the second positive system (310–380 nm) of N₂ (C³Π_u → B³Π_g) and the first negative system (390–440 nm) of N₂⁺ (B²Σ_u⁺ → X²Σ_g⁺).⁴⁴ Additionally, OH (A²Σ⁺ → X²Π) radicals is prominently seen at 309 nm in the spectrum of the gliding arc discharge which plays a crucial role in plasma chemical reactions such as the oxidation of gas and liquid pollutants. The nitric oxide gamma band NO_γ (A²Σ⁺ → X²Π) is observed in 200–280 nm. Reactive oxygen (O) radicals are found at wavelengths 777 nm with electronic transitions 4s(3D)4d → 4p(3P).³⁰ The intensity of the reactive species is decreased while increasing the applied voltage and airflow. The OH formation is markedly observed in the discharge except for "O" and "A" discharge positions.

The different spectral lines of N(III) are used to calculate the electron excitation temperature and electron density. Table III shows the spectral lines with corresponding statistical weight, energy level, and degeneracy of the state. From Eq. (5), we plot the graph of

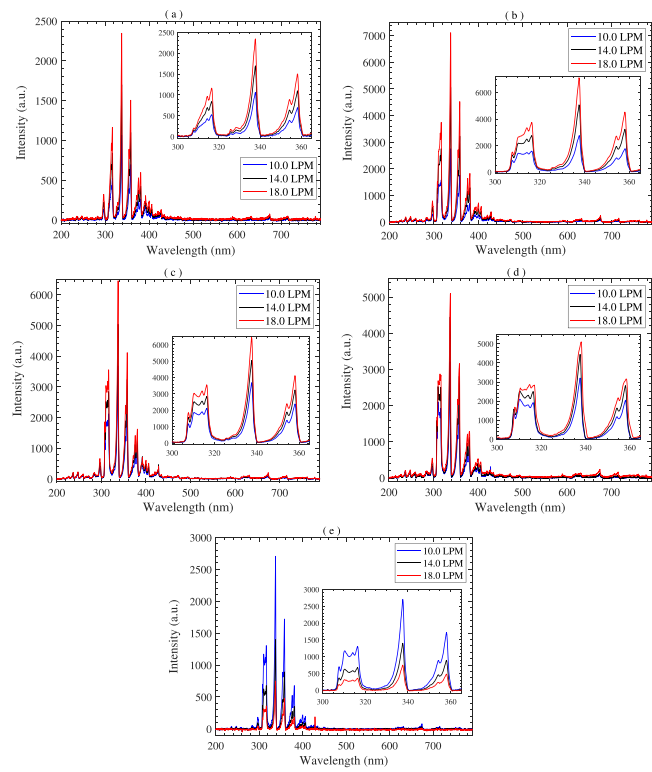


FIG. 9. Optical emission spectrum of atmospheric pressure air gliding arc discharge for different values of airflow rate at different discharge positions: (a) "O" (b) "A" (c) "B" (d) "C," and (e) "D."

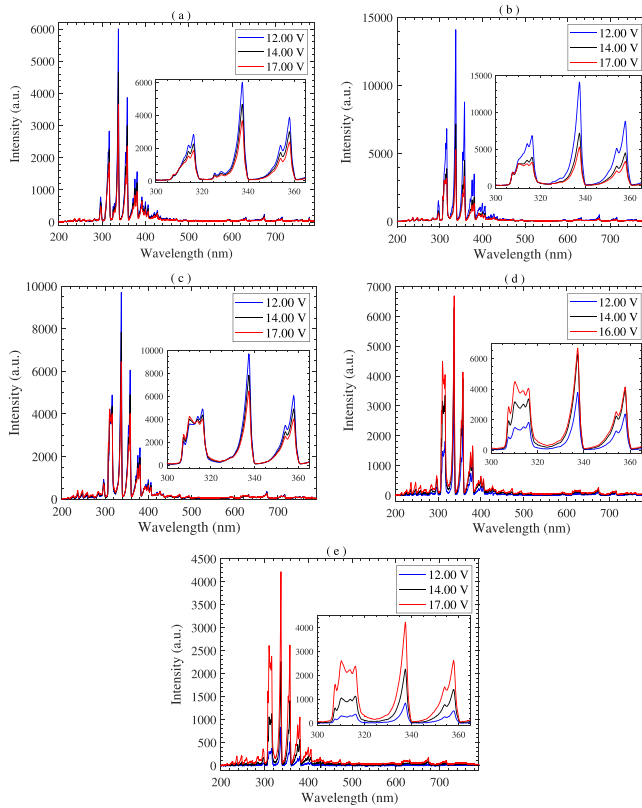


FIG. 10. Optical emission spectrum of atmospheric air gliding arc discharge for different values of applied voltage at different discharge positions: (a) “O” (b) “A” (c) “B” (d) “C,” and (e) “D.”

TABLE III. Observed N(III) peaks in optical emission spectroscopy of GAD and its corresponding spectroscopic data³⁶ for plotting Boltzmann plot.

λ_{ij} (nm)	$A_{ij} (s^{-1})$	E_j (eV)	$g_i - g_j$
336.734	1.27×10^8	39.351 99	6–6
375.467	3.78×10^7	38.957 98	4–6
377.105	5.59×10^7	38.957 98	4–4
393.852	8.96×10^7	41.481 18	4–6
399.863	1.76×10^8	42.495 48	4–6
400.358	1.88×10^8	42.495 60	6–8

In $(\lambda_{ij} I_{ij} / A_{ij} g_j)$ as the function of energy level (E_j), the slope of the linear fitted line gives the electron excitation temperature. The sample Boltzmann plot to determine the electron temperature is depicted in Fig. 11. Once we obtain the electron temperature, the electron density is calculated using Eq. (6). The effect of airflow and applied voltage on electron temperature and density variation at different discharge positions are shown in Figs. 12 and 13, respectively. It is found that electron temperature and density both decrease with the distance from the ignition point of the discharge. The discharge position “O” is the ignition point (breakdown region) and the position “D” is the position 10.0 mm below the end of the electrodes. Immediately after ignition

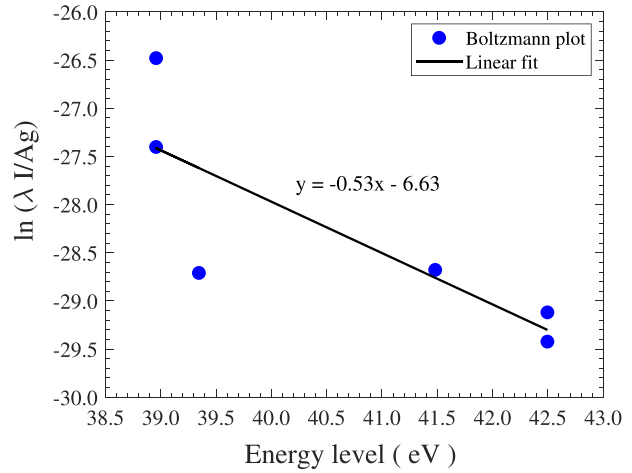


FIG. 11. Sample of Boltzmann plot to determine the electron excitation temperature for gliding arc discharge at 12.00 V applied voltage and 15.0 LPM airflow.

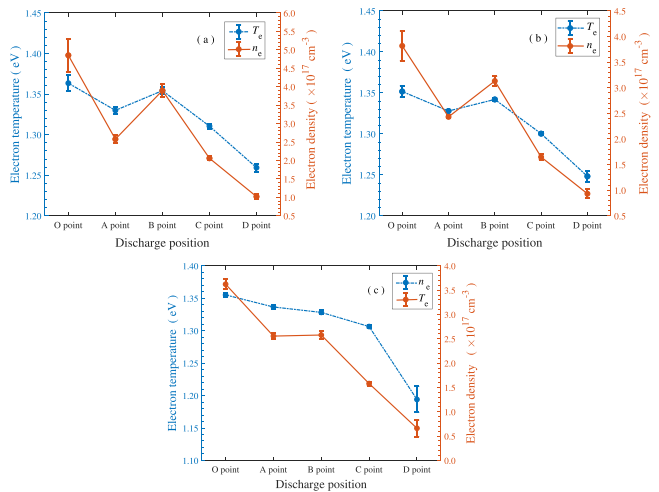


FIG. 12. Variation of electron temperature and density at different discharge positions with constant applied voltage 12.00 V for the different values of airflow rates (a) 10.0 LPM, (b) 14.0 LPM, and (c) 18.0 LPM.

(at position “O”), it is found that the electron temperature and density both decrease toward the outlet (toward the end of electrodes) of discharge. The electron temperature and density are highest at the discharge position “O” for 10.0 LPM airflow [(1.364 ± 0.010) eV and $(4.85 \pm 0.45) \times 10^{17} \text{ cm}^{-3}$] and lowest at position “D” for 18.0 LPM airflow [(1.194 ± 0.024) eV and $(0.66 \pm 0.17) \times 10^{17} \text{ cm}^{-3}$]. It is seen that the electron excitation temperature and density are lowest at the discharge position “D” for all the cases (airflow rate). These obtained parameters (electron temperature and density) are consistent with the previous works.^{45,46} The variation of applied voltage also affects the electron temperature and density of discharge. From Fig. 13, it is seen that the electron excitation temperature and density decrease toward the end of the electrodes, and the maximum is obtained at the discharge position “O” for the applied voltage 20.0 V [(1.442 ± 0.001) eV

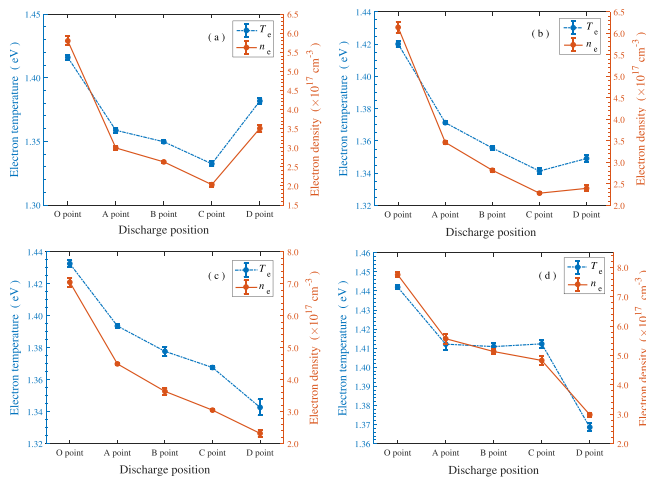


FIG. 13. Variation of electron temperature and density at five different discharge positions with constant airflow rate 15.0 LPM for different values of applied voltage (a) 12.00 V, (b) 14.00 V, (c) 17.00 V, and (d) 20.00 V.

and $(7.75 \pm 0.08) \times 10^{17} \text{ cm}^{-3}$. With the increase in applied voltage, the electron temperature and density are found to be increased.

The rotational and vibrational temperatures of the discharges are calculated using the MassiveOES API. Figure 14 shows the measured and simulated traces of N_2 (C-B) spectra and their residual (differences). The absolute value of the difference (residue) is negligible. During the spectra fit, the residue is minimized by adjusting the wavelength shift and broadening so that minimum residue is achieved.

The effect of air flow rate and applied voltage on the rotational and vibrational temperatures at the different discharge positions are shown in Figs. 15 and 16 respectively. Rotational temperature is a widely used method to determine the transnational (gas) temperature of diatomic molecules in the non-equilibrium plasma.⁴⁷ It is found that both rotational and vibrational temperatures are minimal at the

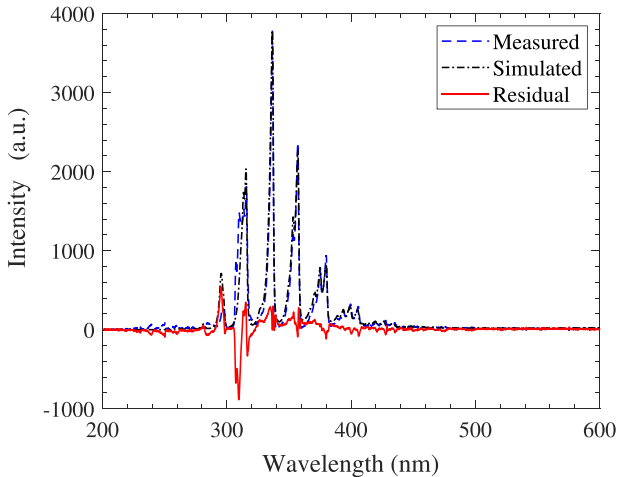


FIG. 14. Measured and simulated trace of spectroscopic data of N_2 (C-B) spectrum obtained using the MassiveOES application programming interface for 12.00 V applied voltage and 15.0 LPM airflow at discharge position "D."

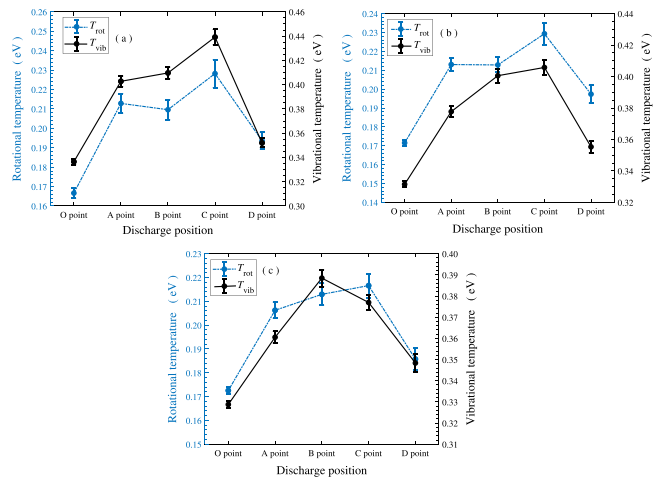


FIG. 15. Variation of rotational and vibrational temperature at different discharge positions with constant applied voltage 12.00 V for different values of airflow rate (a) 10.0 LPM, (b) 14.0 LPM, and (c) 18.0 LPM.

discharge position "O" and gradually increase up to position "C" and beyond that position, they decrease. This is attributed to the fact that the intensity of the plasma decreases beyond the discharge position "C." Thus, the rotational and vibrational temperatures are found to be decreased. Moreover, when the airflow increases, the discharge gets more air to cool and the rotational and vibrational temperatures decrease as well. The minimum rotational and vibration temperature values at the discharge position "O" are (0.167 ± 0.003) and (0.336 ± 0.002) eV, respectively. The variation of applied voltage also affects the rotational and vibrational temperatures. For the gliding arc discharge, both temperatures are found to be increased for the increase in applied voltage. The rotational and vibrational temperatures change from (0.158 ± 0.006) to (0.241 ± 0.007) and (0.312 ± 0.002) to

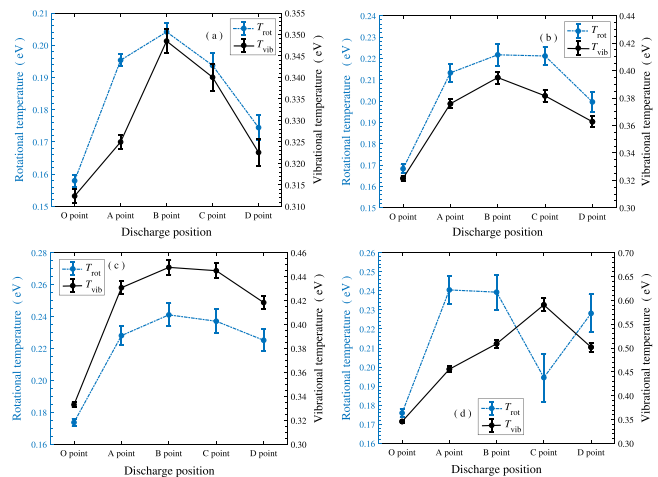


FIG. 16. Variation of rotational and vibrational temperatures at different discharge positions at constant airflow rate 15.0 LPM for different values of applied voltage (a) 12.0 V, (b) 14.0 V, (c) 17.0 V, and (d) 20.0 V.

(0.590 ± 0.014) eV, respectively. The obtained results are consistent with the previous work.⁴⁸

IV. CONCLUSION

We have successfully developed a low-cost power supply using locally available materials, enabling the generation of atmospheric pressure gliding arc discharge for various non-thermal plasma applications. The produced discharge is characterized through comprehensive electrical and optical characterizations. The output voltage (V_{RMS}) of the power source demonstrated a linear increment, ranging from 7.67 ± 0.41 to 26.71 ± 0.88 kV in the absence of load. The airflow positively influenced the arc velocity while applied voltage showed a diminishing effect. The power consumption of the discharge varied from 8.55 to 18.34 W, corresponding to applied voltage changes from 12.00 to 20.00 V. The electron temperature and density of the discharge decrease toward the end of the electrodes. At the outermost non-equilibrium region with an airflow of 18.0 LPM, the electron temperature, and density reached their lowest values, measuring 1.194 ± 0.024 eV and $(0.66 \pm 0.17) \times 10^{17} \text{ cm}^{-3}$, respectively. The electron temperature and density increase for the increase in applied voltage. As the airflow increases, the rotational and vibrational temperatures decrease with maximum temperature at the lowermost equilibrium discharge position. On the other hand, when we increase the applied voltage, the rotational and vibrational temperatures are maximum at the equilibrium discharge position. The resulting values of plasma density and temperature are in the order of gliding arc discharges. Our results demonstrated that a non-thermodynamic equilibrium in the plasma discharges as evidenced by the relationship $T_{\text{exc}} > T_{\text{vib}} > T_{\text{rot}}$. These findings underscore the potential of our assembled power supply to generate low-cost non-thermal equilibrium plasma, providing valuable insights for future research and applications in the field of atmospheric pressure gliding arc discharge.

SUPPLEMENTARY MATERIAL

See the supplementary material for all the data obtained from the experiment that are used to study the primary and secondary voltages

TABLE IV. Variation of primary and secondary RMS voltage of fly-back transformer for different values of input voltage.

S. No.	Input voltage (V)	Primary voltage (V)	Secondary voltage (kV)
1	7.00	10.27 ± 1.05	7.66 ± 0.41
2	8.00	12.72 ± 1.01	9.51 ± 0.45
3	9.00	15.09 ± 1.11	11.35 ± 0.52
4	10.00	17.42 ± 1.09	13.14 ± 0.80
5	11.00	19.91 ± 1.05	14.91 ± 0.74
6	12.00	22.36 ± 1.15	16.52 ± 0.58
7	13.00	24.73 ± 1.19	18.86 ± 0.52
8	14.00	26.95 ± 1.16	20.39 ± 0.49
9	15.00	29.13 ± 1.33	22.13 ± 0.51
10	16.00	31.35 ± 1.16	23.66 ± 0.47
11	18.00	36.02 ± 1.29	25.60 ± 0.62
12	20.00	38.92 ± 1.34	26.71 ± 0.88

TABLE V. Variation of the transitional velocity of gliding arc for different values of airflow rate with constant input voltage 12.00 V.

S. No.	Flow rate (LPM)	Arc velocity (cm/s)
1	10.0	321.3 ± 25.2
2	12.0	443.8 ± 27.3
3	14.0	488.1 ± 26.1
4	15.0	454.1 ± 30.5
6	16.0	461.1 ± 15.1
7	17.0	477.3 ± 23.3
8	18.0	488.1 ± 26.1

TABLE VI. Variation of the transitional velocity of gliding arc for different values of input voltage with constant flow rate 15.0 LPM.

S. No.	Input voltage (V)	Arc velocity (cm/s)
1	12.00	454.3 ± 35.3
2	13.00	432.8 ± 23.8
3	14.00	401.4 ± 19.6
4	15.00	393.1 ± 21.4
6	16.00	323.7 ± 24.3
7	17.00	311.8 ± 21.9
8	18.00	309.6 ± 14.6
9	19.00	287.7 ± 17.2
10	20.00	281.7 ± 15.7

(shown in Table IV), current–voltage characteristics of discharge, arc velocity (shown in Tables V and VI), and optical emission spectra.

ACKNOWLEDGMENTS

We acknowledge the Research Coordination and Development Council, Tribhuvan University, Kirtipur, Nepal, for the National Priority Research Grant (No. TU-NPAR-077/78-ERG-12). Additionally, we would like to express our appreciation to Professor Deepak Prasad Subedi, Dr. Sanju Shrestha, and Mr. Sandesh Devkota for their support during the assembling of the power supply. S. Sharma acknowledges the Research Coordination and Development Council, Tribhuvan University, Kirtipur, Nepal, for the Master of Science Thesis Grant-2078. R. Chalise would like to acknowledge the University Grants Commission, Nepal, for the Ph. D. fellowship (PhD-78/79-S&T-16), and extend special thanks to Dr. Bhagirath Ghimire for his guidance in problem identification and the design of plasma sources.

AUTHOR DECLARATIONS

Conflict of Interest

The authors have no conflicts to disclose.

Author Contributions

Sangat Sharma: Conceptualization (equal); Data curation (equal); Formal analysis (equal); Methodology (equal); Software (equal);

Visualization (equal); Writing – original draft (equal). **Roshan Chalise:** Conceptualization (equal); Data curation (equal); Formal analysis (equal); Methodology (equal); Software (equal); Validation (equal); Visualization (equal); Writing – original draft (equal). **Suresh Basnet:** Data curation (equal); Formal analysis (equal); Methodology (equal); Software (equal); Visualization (equal); Writing – original draft (equal). **Hari Prasad Lamichhane:** Conceptualization (equal); Supervision (equal); Validation (equal). **Raju Khanal:** Conceptualization (equal); Formal analysis (equal); Funding acquisition (equal); Methodology (equal); Software (equal); Supervision (equal); Writing – review & editing (equal).

DATA AVAILABILITY

The data that support the findings of this study are available from the corresponding author upon reasonable request [and its supplementary material].

REFERENCES

- ¹C. j Liu, G. h Xu, and T. Wang, *Fuel Process. Technol.* **58**, 119 (1999).
- ²A. D'Angola, G. Colonna, and E. Kustova, *Front. Phys.* **10**, 39 (2022).
- ³J. S. Chang, P. A. Lawless, and T. Yamamoto, *IEEE Trans. Plasma Sci.* **19**, 1152 (1991).
- ⁴T. Ohta, in *Cold Plasma in Food and Agriculture*, edited by N. Misra, O. Schlüter, and P. Cullen (Academic Press, San Diego, 2016).
- ⁵D. B. Graves, *Phys. Plasmas* **21**, 080901 (2014).
- ⁶O. V. Penkov, M. Khadem, W.-S. Lim, and D.-E. Kim, *J. Coat. Technol. Res.* **12**, 225 (2015).
- ⁷H. Conrads and M. Schmidt, *Plasma Sources Sci. Technol.* **9**, 441 (2000).
- ⁸T. G. Klämpfl, G. Isbary, T. Shimizu, Y.-F. Li, J. L. Zimmermann, W. Stolz, J. Schlegel, G. E. Morfill, and H. U. Schmidt, *Appl. Environ. Microbiol.* **78**, 5077 (2012).
- ⁹H. J. Lee, H. Jung, W. Choe, J. S. Ham, J. H. Lee, and C. Jo, *Food Microbiol.* **28**, 1468 (2011).
- ¹⁰F. Leipold, Y. Kusano, F. Hansen, and T. Jacobsen, *Food Control* **21**, 1194 (2010).
- ¹¹R. Chalise, P. Shrestha, S. Sharma, S. Basnet, L. N. Mishra, and R. Khanal, *J. Phys. D: Appl. Phys.* **56**, 505201 (2023).
- ¹²A. Pudasaini, D. K. Chaudhary, R. Chalise, P. Shrestha, L. P. Joshi, and R. Khanal, *Adv. Mat. Res.* **1176**, 43 (2023).
- ¹³P. Lamichhane, T. R. Acharya, N. Kaushik, L. N. Nguyen, J. S. Lim, V. Hessel, N. K. Kaushik, and E. H. Choi, *J. Environ. Chem. Eng.* **10**, 107782 (2022).
- ¹⁴X. Tu and J. C. Whitehead, *Int. J. Hydrogen Energy* **39**, 9658 (2014).
- ¹⁵A. Czernichowski, *Pure Appl. Chem.* **66**, 1301 (1994).
- ¹⁶O. Mutaf Yardimci, A. V. Saveliev, A. A. Fridman, and L. A. Kennedy, *J. Appl. Phys.* **87**, 1632 (2000).
- ¹⁷Y. Kusano, *Surf. Eng.* **25**, 415 (2009).
- ¹⁸L. Lie, W. Bin, Y. Chi, and W. Chengkang, *Plasma Sci. Technol.* **8**, 653 (2006).
- ¹⁹B. Eliasson and U. Kogelschatz, *IEEE Trans. Plasma Sci.* **19**, 1063 (1991).
- ²⁰F. Zhu, H. Zhang, X. Li, A. Wu, J. Yan, M. Ni, and X. Tu, *J. Phys. D: Appl. Phys.* **51**, 105202 (2018).
- ²¹R. Burlica and B. R. Locke, *IEEE Trans. Ind. Appl.* **44**, 482 (2008).
- ²²M. R. Ghezzar, M. Belhadj, F. Abdelmalek, A. Rais, and A. Addou, *Int. J. Environ. Waste Manag.* **2**, 458 (2008).
- ²³H. S. Kim, Y. I. Cho, I. H. Hwang, D. H. Lee, D. J. Cho, A. Rabinovich, and A. Fridman, *Sep. Purif. Technol.* **120**, 423 (2013).
- ²⁴N. C. Roy, M. M. Hasan, A. H. Kabir, M. A. Reza, M. R. Talukder, and A. N. Chowdhury, *Plasma Sci. Technol.* **20**, 115501 (2018).
- ²⁵S.-H. Hong, T.-H. Kim, and S. Choi, *Appl. Sci. Converg. Technol.* **28**, 101 (2019).
- ²⁶A. Fridman, S. Nester, L. A. Kennedy, A. Saveliev, and O. Mutaf-Yardimci, *Prog. Energy Combust. Sci.* **25**, 211 (1999).
- ²⁷T. A. Hameed and S. Kadhem, *Iraqi J. Sci.* **60**, 2649 (2019).
- ²⁸R. Burlica, M. J. Kirkpatrick, and B. R. Locke, *J. Electrostat.* **64**, 35 (2006).
- ²⁹C. M. Du, Y. W. Sun, and X. F. Zhuang, *Plasma Chem. Plasma Process.* **28**, 523 (2008).
- ³⁰R. Chalise, P. Bhandari, S. Sharma, S. Basnet, D. P. Subedi, and R. Khanal, *AIP Adv.* **13**, 065104 (2023).
- ³¹A. Pressman, *Switching Power Supply Design* (McGraw-Hill Education, 2009).
- ³²A. Costanzo, M. Dionigi, F. Mastri, and M. Mongiardo, in *2013 IEEE Wireless Power Transfer (WPT)* (IEEE, 2013), p. 69.
- ³³S. Zabihi, F. Zare, G. Ledwich, A. Ghosh, and H. Akiyama, *IEEE Trans. Dielectr. Electr. Insul.* **17**, 1901 (2010).
- ³⁴P. Davari, F. Zare, and A. Ghosh, in *2012 7th IEEE Conference on Industrial Electronics and Applications (ICIEA)* (IEEE, 2012), p. 1517.
- ³⁵R. Liao, J. Hao, G. Chen, Z. Ma, and L. Yang, *IEEE Trans. Dielectr. Electr. Insul.* **18**, 1626 (2011).
- ³⁶A. Kramida, Yu. Ralchenko, J. Reader, and NIST ASD Team, *NIST Atomic Spectra Database (Ver. 5.10)* (National Institute of Standards and Technology, Gaithersburg, MD, 2022), <https://physics.nist.gov/asd>.
- ³⁷C. Aragón and J. A. Aguilera, *Petrochim. Acta Part B: At. Spectrosc.* **63**, 893 (2008).
- ³⁸V. K. Unnikrishnan, K. Alti, V. B. Kartha, C. Santhosh, G. P. Gupta, and B. M. Suri, *Pramana* **74**, 983 (2010).
- ³⁹J. Voráč, P. Synek, L. Potočnáková, J. Hnilica, and V. Kudrle, *Plasma Sources Sci. Technol.* **26**, 025010 (2017).
- ⁴⁰J. Voráč, P. Synek, V. Procházka, and T. Hodor, *J. Phys. D: Appl. Phys.* **50**, 294002 (2017).
- ⁴¹J. Voráč, L. Kusýn, and P. Synek, *Rev. Sci. Instrum.* **90**, 123102 (2019).
- ⁴²G. Nersisyan and W. G. Graham, *Plasma Sources Sci. Technol.* **13**, 582 (2004).
- ⁴³S. Huang, T. Li, Z. Zhang, and P. Ma, *Appl. Energy* **251**, 113358 (2019).
- ⁴⁴A. Loftus and P. H. Krupenie, *J. Phys. Chem. Ref. Data* **6**, 113 (1977).
- ⁴⁵B. Indumathy, J. Anantharasimhan, L. Rao, S. Yugesswaran, and P. V. Ananthapadmanabhan, *J. Phys. D: Appl. Phys.* **55**, 395501 (2022).
- ⁴⁶S. P. Gangoli, A. F. Gutsol, and A. A. Fridman, *Plasma Sources Sci. Technol.* **19**, 065004 (2010).
- ⁴⁷C. O. Laux, T. G. Spence, C. H. Kruger, and R. N. Zare, *Plasma Sources Sci. Technol.* **12**, 125 (2003).
- ⁴⁸T.-L. Zhao, Y. Xu, Y.-H. Song, X.-S. Li, J.-L. Liu, J.-B. Liu, and A.-M. Zhu, *J. Phys. D: Appl. Phys.* **46**, 345201 (2013).